CHANNEL MODELS FOR INDOOR WIRELESS TRANSMISSION

P. Sharma, P. Sachetta, C. Thompson and K. Chandra
Center for Advanced Computation and Telecommunications
Department of Electrical and Computer Engineering
University of Massachusetts Lowell
Lowell, MA. 01854

Abstract

In this paper a procedure is given for obtaining the channel impulse response for a rectangular room in terms of image sources. Exact image source strengths are evaluated using the Laplace transform formulation of the Sommerfeld problem. The coherent component of the impulse response is shown to exhibit significant variation is space. The performance of a decision feedback equalizer is examined in this context. The number of feed-forward and feedback taps required for a prescribed performance level is shown to be strongly influenced by the transmission frequency and source/receiver position.

1. Introduction

Third and fourth generation wireless standards outline support for multimedia data transmission at rates ranging from 2 to over 100 Mb/s. Wireless local area networks and local multipoint distribution systems will operate in the *Ghz* frequency band, providing large bandwidths for voice, video and data delivery. At these carrier frequencies and bandwidths the role of multiple scattering, diffraction and absorption by objects along the transmission path is an important consideration. These channel effects are manifest in the channel impulse response(CIR) or equivalently the multipath power delay profile. A number of studies have been devoted to finding the structure in these responses. These include experiments [1], statistical models fit to measurement results [2], computational approaches using ray-tracing algorithms [3,4] and finite-difference time-domain methods (FDTD) [5].

The CIR structure determines the amount of inter-symbol interference (ISI) present in the received signal. For transmissions in a room the most important reflections that impact ISI result from early arrivals. These arrivals are typically the result of reflections from the walls, floor, and ceiling and the standard accoutrements within the room. These reflected waves occur in rapid succession creating the initial shape of the impulse response. The early arrivals in the impulse response may be considered as coherent and are affected by the receiver and/or transmitter motion. On the other hand the tail of the channel impulse response is incoherent. In this region the response is the result of large numbers of boundary collisions. These channel characteristics are determined by the resonant frequencies and modal damping of the room.

The coherent response which corresponds to early arrivals in the CIR is chiefly responsible for performance degradation from ISI. The performance of adaptive equalizers in indoor channels has been examined in a number of studies. Frigon *et al*. [6] note that even when a line-of-sight path exists between the source and receiver, an equalized system outperforms an unequalized system.

The channel models developed in this work will allow the evaluation of equalizer performance in relation to the room parameters. In particular the degree of spatial variation of the coherent response and its influence on error cancellation will be examined. The CIR of an empty room yields the longest time duration over which coherent wave reflections can be sustained. The presence of fixed and/or moving scatterers in the channel will reduce this time interval. The CIR of an empty room therefore provides an estimate of the worst-case time-dispersive features of the channel.

Section 2.0 presents an algorithm for estimating the indoor room impulse response using the image method. Section 3.0 presents the results under subband filtering and examines the variation of the channel response with source/receiver position and transmission frequency. Section 4.0 discusses the requirements on the equalizer tap lengths for channel estimation and the impact of the coherent and diffuse regions on performance of decision feedback equalizers. Section 5.0 concludes the paper.

2.0 Channel Impulse Response

The computational model proposed is based on the method of images. The image based solution to the channel impulse response is an approximation to the exact solution of wave equation . It approaches the exact solution as the walls of the room approach rigid conditions. This method can provide better time granularity than ray trac-

ing methods for analyzing performance of high bit rate transmissions.

Image based methods are based on similar geometric principles as ray tracing but with corrections for the image source amplitude given by Sommerfeld [7] in 1909. Recently exact image theory has been presented for the electric [8] and magnetic [9] dipole cases. In this method, the walls of the enclosure are replaced by point sources of varying strength and location. The component amplitude of each image is chosen such that the transverse electric and magnetic fields are continuous across the boundary. The image source in these cases is the sum of a point source having an amplitude equal to the plane-wave reflection coefficient and a surface wave term. The surface wave term may be neglected in the image solution if the distance between the source and observation point is greater than a quarter of a wavelength. Operational frequencies in wireless applications typically satisfy this constraint. The number of images required for a impulse response of length T is $O(c^3T^3/V)$ where V is the volume of the room to be modeled. As we can see the number of images increases as t^3. For non-rectangular enclosures comprised of m polyhedral surfaces the number of images generated is $O(m^k)$ to accommodate k reflections, but most of these do not contribute to the field at the observation point. Borish [10] has outlined a criterion for pruning the image source tree. Therefore the image method allows for high time resolution in the impulse response with the disadvantage that it can be compute intensive.

In the case of indoor propagation absorption at the walls is the dominant factor. In the absence of highly-conductive structural elements, the average energy absorption over the solid angle of the walls is high for indoor environments. Hence the amount of reflected energy is low. For a concrete-block wall having complex permittivity $\varepsilon_r = 3.0 + j2 \times 10^{-3}/(\varepsilon_o \omega)$ the energy absorption coefficient $\alpha = 0.88$ at $30Ghz$. For weak reflection conditions Holloway *et al*. [11] have shown that the envelope of the power decay profile at time nt_c in a room satisfies $P(nt_c) = A(1-\alpha)^n/n^2$ where $t_c = 16V/(Sc)$, V is the volume of the room, S is the reflective surface area and $P(0) = A$. The result is simply the $1/r^2$ power contributed by an image located at a distance equal to n times the mean free path between reflections, $l_c = 8V/S$. Using this result the time nt_c required for the power response to fall $60dB$ is approximately $-6t_c/\log_{10}(1-\alpha)$. Therefore much fewer images of $O(-6^3/\log_{10}^3(1-\alpha)l_c^3/V)$ are required.

The impulse response for dissipative walls in a rectangular room will be obtained using a model based on the method of images. An electric dipole is placed at location $\underline{x}^s$ in a rectangular room which has the dimension L_j for the j^{th} coordinate direction. The orientation of the dipole source is given by the unit vector $\underline{u}$. The relative dielectric constant of each of the six walls is considered homogeneous in space and is given by the relative dielectric constant $\varepsilon_j^{(1)}$ and $\varepsilon_j^{(2)}$. Variables with the superscript (1) are located on the walls closest to the origin of the coordinate axis. The electromagnetic wave propagates from the source to an observer located at $\underline{x}$. The evolution of the wave in space and time will be described in terms of the Hertz vector $\underline{\Pi}$.

The component amplitude f_j of each image is chosen such that the transverse electric and magnetic fields are continuous across the boundary. For a point source located at $\underline{x}^s$ the j^{th} component of the Hertz potential at the observation point $\underline{x}$ is given by the expression

$$\Pi_j(\underline{x}, \underline{x}^s, t) = \sum_{\underline{K}} \frac{f_j\left(\frac{ct}{X_{\underline{K}}} - 1, \underline{K}\right)}{X_{\underline{K}}} \tag{1}$$

where c is the speed of light and $X_{\underline{K}} = |\underline{x} - \underline{x}^i(\underline{K})|$ is the distance between the observation point and the $\underline{K}^{th}$ image. The location of each image is given by the coordinate position $\underline{x}^i(\underline{K}) = (x_1^i(K_1), x_2^i(K_2), x_3^i(K_3))$. Each image location can be ordered by its distance from the origin by expressing each component of the image location as

$$x_j^i(K_j) = 2\left[\frac{K_j}{2}\right]_{ceil} L_j + (-1)^{K_j} x_j^s$$

for $K_j = (-\infty, \infty)$. This mapping allows one to unroll the requisite summation. The image position $\underline{x}^i(\underline{K})$ at index $\underline{K} = (0,0,0)$ corresponds to the source point $\underline{x}^s$.

The reflected wave from each wall is evaluated iteratively. The vector Fourier amplitudes of the reflected waves from two planar boundaries located at $x_1 = 0, L_1$ resulting from the image source at $(K_1, 0, 0)$ is

$$\begin{bmatrix} R_1^{K_1} \\ R_2^{K_1} \\ R_3^{K_1} \end{bmatrix} = \begin{bmatrix} N_1^{K_1} & N_2^{K_1} & N_3^{K_1} \\ 0 & N_2^{K_1} & 0 \\ 0 & 0 & N_3^{K_1} \end{bmatrix} \begin{bmatrix} R_1^{-K_1+sgn\,(K_1)} \\ R_2^{-K_1+sgn\,(K_1)} \\ R_3^{-K_1+sgn\,(K_1)} \end{bmatrix} \tag{2}$$

where R_j^0 is equal to the components of the unit vector u_j defining the orientation of the dipole source. The horizontal components in the x_2 and x_3 directions have the index

(2) and (3) whereas the vertical component is given by the index (1). The vector amplitude of the Hertz potential in this case is equal to $(R_1^{K_1}, R_2^{K_1}, R_3^{K_1})$. The reflection coefficient for the remaining planar boundaries are

$$\begin{bmatrix} R_1^{K_2} \\ R_2^{K_2} \\ R_3^{K_2} \end{bmatrix} = \begin{bmatrix} N_1^{K_2} & 0 & 0 \\ N_1^{K_2} & N_2^{K_2} & N_3^{K_2} \\ 0 & 0 & N_3^{K_2} \end{bmatrix} \begin{bmatrix} R_1^{-K_2+sgn\,(K_2)} \\ R_2^{-K_2+sgn\,(K_2)} \\ R_3^{-K_2+sgn\,(K_2)} \end{bmatrix} \tag{3}$$

$$\begin{bmatrix} R_1^{K_3} \\ R_2^{K_3} \\ R_3^{K_3} \end{bmatrix} = \begin{bmatrix} N_1^{K_3} & 0 & 0 \\ 0 & N_2^{K_3} & 0 \\ N_1^{K_3} & N_2^{K_3} & N_3^{K_3} \end{bmatrix} \begin{bmatrix} R_1^{-K_3+sgn\,(K_3)} \\ R_2^{-K_3+sgn\,(K_3)} \\ R_3^{-K_3+sgn\,(K_3)} \end{bmatrix} \tag{4}$$

The function $N_j^{K_m}$ is determined by evaluating the integral

$$N_j^{K_m} = 2\omega\,\mathrm{Re}\left[\int_0^\infty \frac{G(q\omega, \omega, \varepsilon)}{\Delta_m}\, e^{i\omega(\Delta_m - 1)} dq\right]$$

$$G(p, \omega, \varepsilon) = \begin{cases} \text{for } m = j\text{:} \\ \dfrac{\varepsilon - 1}{\varepsilon + 1}\left(\delta(p) + \dfrac{\varepsilon\gamma}{2}\, e^{-\gamma p}\right) - \varepsilon\gamma \displaystyle\int_0^\infty e^{-\gamma|p-s|}\, \frac{J_2(s)}{s}\, ds \\ \textit{otherwise}\text{:} \\ -2\,\dfrac{J_2(p)}{p} \end{cases}$$

where

and $\Delta_m = \sqrt{1 - q^2/(\varepsilon - 1) + i\, 2q\cos\theta_m/\sqrt{\varepsilon - 1}}$. The angle θ_m is the angle between the observation position $\underline{x}$ and the image position vector comprised of the single component $x_m^i(K_m)$ and $\gamma = 1/\sqrt{\varepsilon^2 - 1}$. The frequency parameter ω is equal to the nondimensional wavenumber. The relative dielectric constant ε equals $\varepsilon_m^{(2)}$ when $K_m < 0$ and $\varepsilon_m^{(1)}$ when $K_m > 0$.

Considering all the images the Fourier transform of the $\underline{K}$ image yielding the j^{th} component of the Hertz vector is

$$F_j(\omega, \underline{K}) = R_j^{K_1} R_j^{K_2} R_j^{K_3} \tag{5}$$

Inverting the transform yields the causal signal

$$f_j(t\,\frac{c}{X_{\underline{K}}}, \underline{K}) = \int_0^\infty F_j(\omega, \underline{K}) e^{-i\omega t \frac{c}{X_{\underline{K}}}}\, d\omega \tag{6}$$

The impulse response between the source and observation position is therefore given by the convolution of the reflection coefficients and time shifted time functions. The denominator $X_{\underline{K}}$ in Eqn. (1) reflects the decay in amplitude with distance that results from the spherical spread of the field generated by the image source. Ideally one would like the signal at the observation point to be simply a time-shifted version of the input signal. However, wall reflections serve to distort the signal by superposing both weighted and time shifted versions of the original signal.

A discrete-time representation of the impulse response given in Eqn. (1) can obtained by sampling the waveform in time at intervals of T_s, $t = nT_s$. This corresponds to a spatial sampling at intervals of cT_s. Hence the nondimensional distance between the source and the $\underline{K}$ image is

$$M_{\underline{K}} = X_{\underline{K}}/(cT_s)$$

The $j-th$ component of the electric field E_j for discrete time and space is

$$E_j(\underline{x}, \underline{x}^s, n) = \sum_{p=1}^{3} \sum_{\underline{K}} \frac{\cos(\beta_j)cos(\beta_p) - \delta_{jp}}{M_{\underline{K}}} \left(\ddot{f}_p(n/M_{\underline{K}} - 1, \underline{K}) \right. \tag{7}$$

$$\left. + \frac{\dot{f}_p(n/M_{\underline{K}} - 1, \underline{K})}{M_{\underline{K}}} + (3 - \delta_{jp})\, \frac{f_p(n/M_{\underline{K}} - 1, \underline{K})}{M_{\underline{K}}^2} \right)$$

where $\cos(\beta_j) = (x_j - x_j^i(\underline{K}))/X_{\underline{K}}$, $\dot{f}$ and $\ddot{f}$ correspond to the first and second derivatives with respect to the function's argument.

2.1 CIR Result

A room of dimensions $\underline{L} = (5.4, 3.3, 2.4)$ meters was considered. The source position is $\underline{x}^s = (1.0, 1.0, 1.5)$ meters and the vector orientation of the source and receiver is $\underline{u} = (1, 0, 0)$. The walls of the enclosure have a a constant relative dielectric contrast of $\varepsilon_j^{(1)} = 3.0$ and $\varepsilon_j^{(2)} = 3.0$. The sampling interval was chosen to be $T_s = 0.1$ ns. The impulse responses at two locations are discussed first. Figs. 1(a) and (b) show the wideband impulse responses computed using the image method in Eqn (1) at receiver locations A: $\underline{x} = (1.5, 1.45, 1.5)$ and B: $\underline{x} = (4.95, 2.65, 1.5)$ respectively. The figures show the magnitude of the electric field at the observation point. Three distinct regions of the impulse response may be identified. The first point depicts the arrival of the transmitted signal through the direct line-of-sight path, where the time delay corresponds to the time of flight between the source and receiver. The second region is the coherent regime composed of the arrival of signals reflected from

the walls, floor and ceiling. The amplitude of the impulse response in this region is controlled by the spatial location of the image sources. The electric field of each image source decays asymptotically as $1/t^2$ with time and as $1/X_{\underline{K}}$ with distance from the observation point. Hence the initial pulse amplitudes in the response decay as $1/n$. A comparison of Figs. 1(a) and (b) show that the early arrivals of the coherent regime at location A exhibit stronger amplitudes due to their interaction with the direct path. As the distance from the source increases these amplitudes decrease but when in proximity to the walls their rate of arrival is substantially greater. The third regime corresponds to the later arrivals that travel over multiply reflected paths. Successive convolutions of the reflected wave result in the exponential decay of the impulse response at long time delays. The pattern of variations in this regime is found to be independent of the receiver location. The rate of decay in the diffuse component will however be determined by the magnitude of the relative dielectric contrast of walls. As the contrast decreases so does the energy contributed by the diffuse regime.

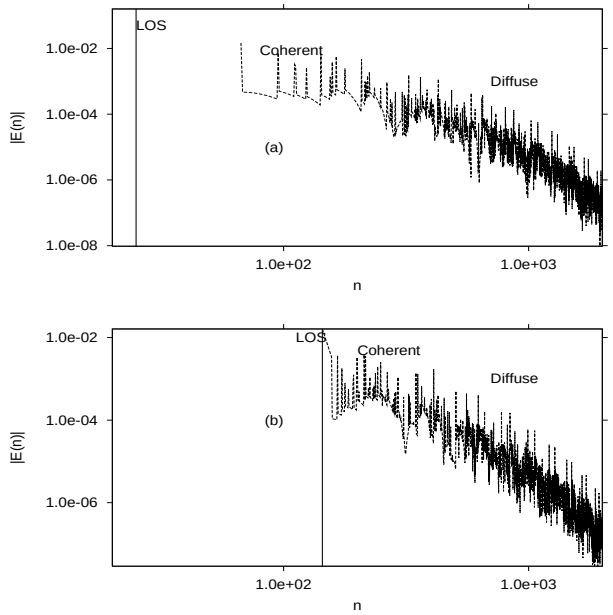

Figure 1: Impulse Response $|\underline{E}|$ verus $n = t/T_s$
(a)Location A, (b)Location B

3.0 Subband Model of the Impulse Response

The N point impulse response from wideband analysis is decomposed into M critically sampled signals using a M –band pseudo quadrature mirror filter (QMF) bank [12]. The filtered signals are then down sampled by a factor of M. Critical sampling results in M base-band signals having a duration of N/M samples. This reduces the complexity of the model for parameter fitting by a factor of M at the outset. In the results presented here $M = 32$ subbands were chosen. This leads to a bandwidth of 161 Mhz for each subband.

The subband impulse responses for the 5^{th} subband are depicted in Figs. 2(a) and 2(b) corresponding to receiver locations A and B respectively. The signal may be considered as the demodulated response signal having a carrier frequency of 0.85 Ghz. At location A where the receiver is closer to the source, high amplitude arrivals occur in quick succession as seen by the two paths at locations 10 and 11 on the time axis. In comparison, only one dominant early arrival occurs at location B. However, the amplitudes of later arrivals are stronger for location B and contribute towards the postcursor section of the impulse response. The maximum absolute amplitude of the impulse response is assumed to separate the pre and postcursor sections of the CIR. The percentage values labelled in Fig. 2 denote the energy contributed by each of these sections. The almost equal split of the energy in the two sections and almost equal amplitudes in succession at location A induces significant problems in error control. The influence of change in transmission frequency may be observed in Figs 2(c) and 2(d) which show the result for the 10^{th} subband corresponding to a carrier frequency of 1.7 Ghz. For this case, the contribution of the pre and post cursor sections are comparable at location B. These features impose spatial variations in the error performance of an equalizer.

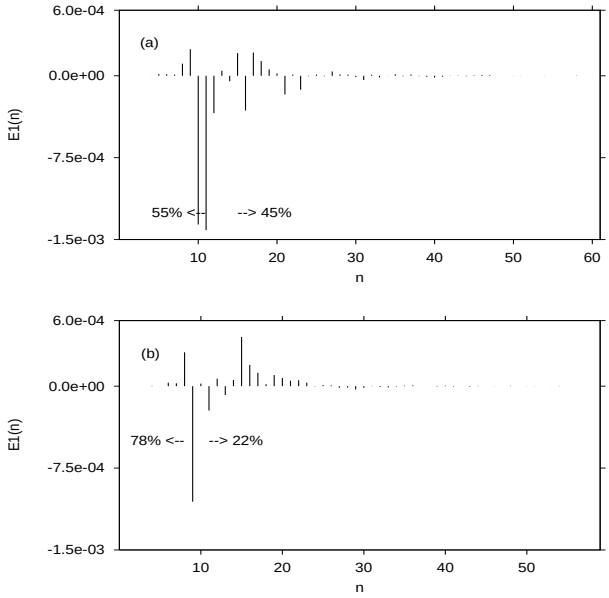

Figure 2(a-b): Impulse Response E_1 from the 5^{th} subband.
(a)Location A, (b)Location B

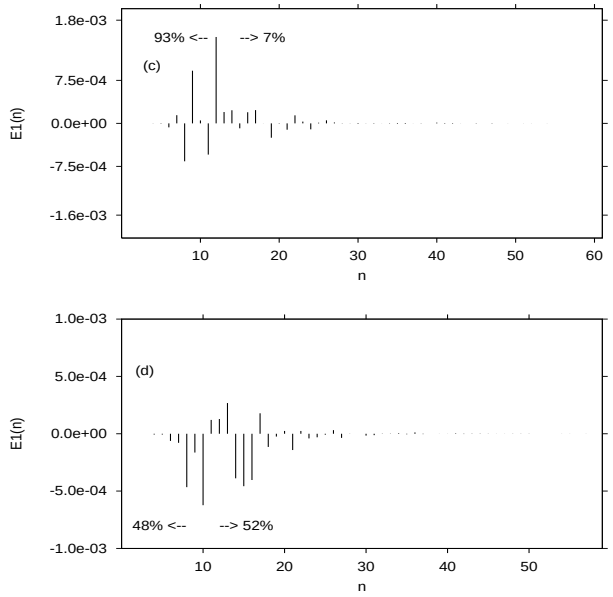

Figure 2(c-d): Impulse Response E_1 from the 10^{th} subband. (c)Location A, (d)Location B

4.0 Performance of Adaptive Equalizers

The DFE has been shown to provide good error rate performance on channels having spectral nulls. A DFE contains two transversal filters that perform feed-forward (FF) and feedback (FB) operations. The feed-forward section compensates for the precursor section that precedes the maximum value in the CIR. The feedback section is designed to eliminate the effects of the postcursor section which comprises of the upper tail of the CIR. The least-mean-squares (LMS) algorithm is chosen for adaptively training the tap coefficients.

The performance of the equalizer depends on the number of FF and FB taps and the step-size parameter μ. For the channel impulse responses examined in this work the bit error rate (BER) was estimated through simulation. BPSK encoded symbols were generated at a rate corresponding to the critical sampling rate of the CIR which was 3.2 nanoseconds. The sampling rate at the equalizer was set equal to the symbol rate. A training sequence length of duration 25 microseconds was found to be sufficient to train the equalizer with $\mu = 10^{-4}$. A total of 5.0 million data symbols were generated for each combination of signal to noise ratio (SNR), FF and FB taps. The results are shown for an peak SNR of 12 decibels. In each case, the performance is determined by varying the FF and FB taps. Figs. 4(a) and (b) show the BER as a function of number of FB taps for choices of $FF = 5, 12, 25, 35$ for the channels shown in Fig. 2(a) and (b) respectively. The channel for location *A* exhibits slow convergence with increase in FF taps. More than 25 taps are required for the error to decrease to 10^{-3} level. About $10 - 15$ FB taps were found to be the adequate for most cases. Fig. 4(b) depicts the results for location *B*. The error is insensitive to increase in FF value, requiring only 5 taps for convergence of BER to the 10^{-6} level.

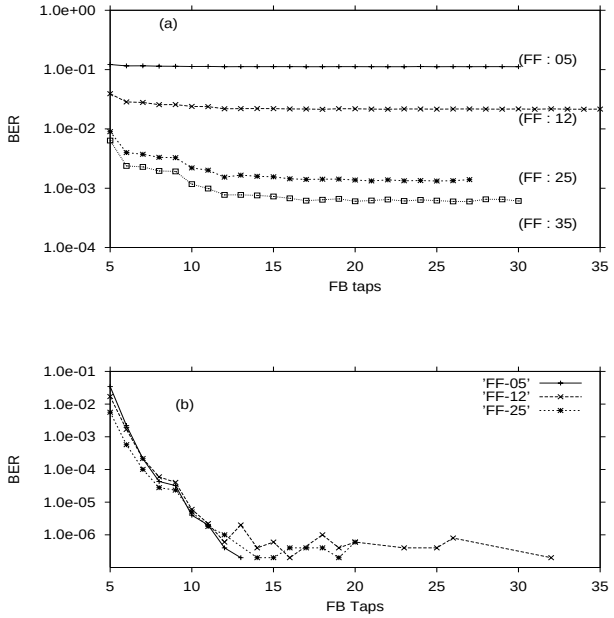

Figure 4(a-b): BER vs number of FB taps for CIR in Figs. 2(a-b). $SNR = 12dB$.

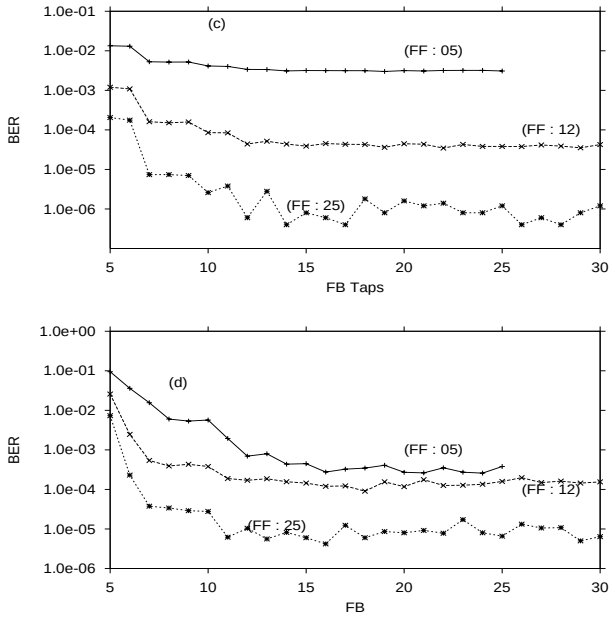

Figure 4(c-d): BER vs number of FB taps for CIR in Figs. 2(c-d). $SNR = 12dB$.

The results for the CIR's shown in Figs. 2(c) and (d) are depicted in Figs. 4 (c) and (d) respectively. In contrast to the first case, both locations require large FF tap lengths. For location *A* the dominant channel power resides in the precursor section. A FF tap length of 25 or more is required to compensate this effect. The saturation level of the error-rate occurs at 10^{-6}. In comparison, the results in Fig. 4(d) for location *B* show higher error levels of 10^{-5}. This may be attributed to sizeable energy in the post-cursor section which produces noise enhancement. The sample of results discussed show the importance of accurate representations of the CIR for achieving spatially uniform error performance. The rate of occurrence of the early arrivals and strength of their amplitudes determine the length of the feed-forward tap length. The post-cursor section of the impulse response exhibits relatively homogeneous variation in space requiring on the order of $10-15$ feedback taps. The bit error rate saturates at a level that is a function of the power in the diffuse component of the impulse response.

5.0 Conclusions

The spatial variation of the impulse response of a rectangular room is shown to exhibit significant variation in its coherent component. This feature impacts the choice of the parameters of an adaptive equalizer. At locations near the source, the interaction of the direct and reflected paths increase the power in the precursor section of the channel impulse response. This feature requires an increase in the number of DFE feed-forward taps. As the receiver moves away from the source the span of the coherent component expands requiring an increasing number of feedback filter coefficients. The channel models obtained for the empty room allow an assessment of error control schemes with spatial variation. These models also serve as baseline reference models to be evaluated under the influence of changes in the channel environment.

Acknowledgements: This work was supported in part by the National Science Foundation under the grant ANI-9734585.

References

1. A. M. Hammoudeh and G. Allen, "Millimetric wavelengths radiowave propagation for line of sight indoor microcellular mobile communications," IEEE Trans. Vech. Tech., vol. 44, 446-460, 1995.

2. A. A. Saleh and R.A. Valenzuela, "A statistical model for indoor multipath propagation," IEEE J. Select. Areas Commun., vol. 5, 128-137, 1987.

3. U. Derschm, J. Troger and E. Zollinger, "Multiple reflections of radio wave in a corridor," IEEE Trans. Ant. Prop., vol. 42, 1571-1574, 1994.

4. G. Yang and K. Pahlavan, "Analysis of multi carrier modems in an office environment using 3D ray tracing," Proc. IEEE GLOBECOM 94, p42046, San Francisco, CA., 1994.

5. A. Lauer, I. Wolff, A. Bahr, J. Pamp, J. Kunisch and I. Wolf, "Multimode FDTD simulations for indoor propagation including antenna properties, " Proc. 1995 IEEE 45th Veh. Tech. Conf., p454-458, Chicago, IL., 1995.

6. J.-F Frigon, B. Daneshrad, J. Putnam, E. Berg, R. Kim, T. Sun, and H. Samueli, "Field trial results for high-speed wireless indoor data communications," IEEE J. Select. Areas Commun., vol. 18, 297-309, 2000.

7. A.N. Sommerfeld, "Propagation of waves in wireless telegraphy," Ann. Phys. (Paris), 28, p665-736, 1909.

8. V. Lindell and E. Alanen, "Exact image theory for the Sommerfeld half-space problem, part I: vertical magnetic dipole," IEEE Trans. on Ant. and Prop., vol. 32, 126-133, 1984.

9. V. Lindell and E Alanen," Exact image theory for the Sommerfeld half-space problem, part II: vertical electric dipole," IEEE Trans. on Ant. and Prop., vol. 32, 841-847, 1984.

10. J. Borish, "Extension of the image model to arbitrary polyhedra," J. Acoust. Soc. Am., vol. 75, 1827-1836, 1984.

11. L. Holloway, M.G. Cotton and P. McKenna, "A model for predicting the power delay profile characteristics inside a room," IEEE Trans. Veh. Tech., vol. 48, 1999

12. R.V. Cox, "The Design of uniformly and nonuniformly QMF," IEEE Trans. Signal Proc., vol. 34, 1090-1096, 1986.